

Robotic deposition of 3d nanocomposite and ceramic fiber architectures via UV curable colloidal inks

Yoram de Hazan^{a,*}, Madlen Thänert^{a,b}, Martin Trunec^c, Jiri Misak^{a,c}

^a *Laboratory for High Performance Ceramics, Empa, Swiss Federal Laboratories for Materials Science and Technology, Überlandstrasse 129, CH-8600 Dübendorf, Switzerland*

^b *Hochschule für Technik und Wirtschaft, Friedrich-List-Platz 1, 01069 Dresden, Germany*

^c *Institute of Materials Science and Engineering, Faculty of Mechanical Engineering, Brno University of Technology, Technická 2, Brno 616 69, Czech Republic*

Received 21 September 2011; accepted 5 December 2011

Available online 11 January 2012

Abstract

A novel approach for producing predetermined, complex 3d ceramic architectures by robotic deposition where UV radiation is used for solidification is presented. Homogeneous, highly loaded, solvent free colloidal inks with controlled viscoelastic properties are achieved by proper selection of monomers and surfactants. Room temperature deposition of complex 3d fiber networks having filaments in the 100 μm range is demonstrated for Al_2O_3 and hydroxyapatite model particles for structural and biomedical applications. Solidification of the structures by UV radiation allows additional shaping of the structures by post-printing processes such as cutting, folding and bonding. 2d and 3d architectures with high aspect ratios retain their shape and transform to macroscopic ceramics after thermal debinding and sintering procedures. Sintered alumina fiber networks functionalized with a 3–5 μm layer of TiO_2 nanoparticles exhibit photocatalytic activity for the decomposition of formaldehyde as a similar weight of loose powder, indicating possible applications in catalytic reactors prototypes.

© 2011 Elsevier Ltd. All rights reserved.

Keywords: Shaping; UV; 3d robotic deposition; Fiber network; Hydroxyapatite

1. Introduction

Over the last 30 years a variety of computer aided manufacturing technologies for producing predetermined 3d polymer, metal and ceramic architectures by additive manufacturing techniques have emerged. These include stereolithography (SLA), selective laser sintering (SLS), 3d inkjet printing (3DP), laminated object manufacturing (LOM), and direct write techniques (DW).^{1–5}

Among the new and promising direct write technologies is the 3d robotic deposition,^{4–22} which is sometimes referred to as robocasting,⁴ 3d fiber deposition,⁸ or extrusion free forming.⁹ The technology has potential for a wide variety of applications in biomedicine,^{14–19} light porous structures,⁸ catalysis,^{11,12} as

well as sensors and MEMS.^{7,20,21} In contrast to commercial techniques such as SLA and 3DP the 3d robotic deposition technique allows direct assembly of predetermined and complex 3d fiber networks in the micrometer scale with self-supporting features. The cross section of the fiber can also be controlled by the deposition nozzle.^{13,14}

3d robotic deposition technologies use various materials and solidification methods. These include coagulation of oppositely charged colloids,^{4,5} coagulation solutions,⁵ freezing,⁶ or sol–gel transition.⁷ 3d fiber networks composed of filaments with dimensions around 100 μm and spanning gaps as large as 2 mm have been demonstrated.^{4,5}

Most recently, new technologies which employ direct UV illumination for solidification of continuous filaments have emerged.^{18,21–25} The ability to perform rapid and local UV curing adds great flexibility to the robotic deposition process. The first demonstration of combined UV-curing with 3d robotic deposition for producing hydrogel scaffold was made

* Corresponding author. Tel.: +41 43 305 9168; fax: +41 43 305 9168.

E-mail addresses: ydehazan@bluewin.ch, ydehazan@gmail.com (Y. de Hazan).

by Barry et al.¹⁸ An innovative contribution to the technology was presented by Lebel et al. who demonstrated fabrication of microcoils from CNT/SiO₂/polymer nanocomposites.²¹ Another important development was the spinning of continuous fibers and fiber networks from highly loaded, colloidal ceramic dispersions which are UV cured ‘on the fly’.^{23–25}

Conceptually, there are two distinct ways to produce 3d fiber architectures by robotic deposition of UV curable inks. In the first, the extruded filament is exposed to continuous and local UV curing.^{18,21} This approach where the curing and extrusion steps are ‘coupled’ works well for rapid shape stabilization of self-supported structures (e.g. coils).²¹ In the second approach which is employed in this work, the extrusion and UV curing are decoupled. This approach is better suited for multilayers where a good interface between layers is required. The extrusion is stopped after deposition of every 1–2 layers allowing for a UV curing step. Here, in contrast to the first approach, bonding between fiber layers is much easier to control since there is at least one uncured layer at an interface during curing. Nevertheless, a process where the extrusion and curing are decoupled impose more stringent requirements on ink rheology (i.e. shape retention of filaments).

In this work we focus on solvent free, monomer (or oligomer) based ink systems such as those used in stereolithography.² These enable highly loaded colloidal ceramic inks and good interface properties between layers.^{2,3,23–26} At the same time such compositions outlined above pose new and interesting challenges for printing of filaments, since they require very different rheological characteristics compared to fluids used in stereolithography. The most critical one is obtaining an ink with high solid loading which is well dispersed and exhibiting simultaneously high elastic modulus and yield point which are necessary for shape retention of the extruded filament. The rheology of pure or lightly filled polymer based inks is primarily dependent on the polymer host which exhibits appropriate viscoelastic properties.^{18,21} However, higher solid loadings necessary for macroscopic ceramics require the addition of diluents which introduces a drying step, or spinning of melts at elevated temperatures and pressures where the added value of UV curing would be diminished. High solid loading can be achieved in a low viscosity monomer/oligomer medium.²⁶ Such medium does not provide viscoelasticity without strong particle–medium and/or particle–particle interactions. These in turn limit the maximal solid loading since well dispersed colloidal inks require low particle–particle interactions. In order to achieve highly loaded, homogeneous printable inks it is therefore necessary to find an optimum for particle–particle and particle–medium interaction via careful choice of monomer/oligomer and surfactant system.

In this work the production of predetermined, complex 3d ceramic/polymer nanocomposite fiber networks by robotic deposition of high loaded, solvent free UV curable ceramic colloidal inks is demonstrated and discussed in length. A brief demonstration has already been presented elsewhere.²² Al₂O₃ and hydroxyapatite (HA) are used as model particles to demonstrate feasibility for structural and biomedical applications, respectively. The use of post-printing shaping processes such as folding and bonding is illustrated. The transformation of the

nanocomposite fiber architectures to macroscopic ceramics via thermal debinding and sintering processes is presented.

2. Experimental

2.1. Materials

TMDAR (Taimei Chemical Co., Ltd., Japan), α -Al₂O₃ with an average particle size of 150 nm and a specific surface area (SA) of 12.5 m² g⁻¹, and hydroxyapatite (HA, Sigma–Aldrich 04238 – puriss.) with SA of 67 m² g⁻¹ were used as model ceramic colloidal particles. The surface area was measured by the BET method with SA3100 (Beckman Coulter, USA) after drying the powders at 180 °C for 2 h under N₂ flow. Both particles were used as received. TiO₂ nanoparticles (Aerosil P25) with a surface area of 50 m² g⁻¹ were obtained from Evonik, Germany.

The UV curable monomers/oligomers used in this study are listed in Table 1 along with details of the manufacturer, chemical formula and density. 4-HBA and PEGDA monomers were used in previous studies as media for low viscosity, high solid loading, UV curable colloidal ceramic dispersions and demonstrations of fiber spinning methods.^{23–26} Bisphenol A diacrylate (BPADA) was investigated as a high viscosity monomer (900–2000 Pas at 25 °C).

Polyethylene glycol methacrylate (PEGMA) with a molecular weight of 360 g mol⁻¹ was also studied. The surfactant used in this work for both particles is 2-[2-(2-methoxyethoxy)ethoxy] acetic acid (TODS). The surfactant which consists of an adsorbing carboxylic acid group and a relatively short ethylene oxide tail has proven successful in dispersing nanoparticles such as indium tin oxide (ITO).²⁷ In effect it is a single molecule analog of the commercial comb-polyelectrolytes used previously^{23–26} but simpler to use since it can be added directly to the particle monomer mixture. MelPers4343, a commercial comb polyelectrolyte surfactant from BASF (Ludwigshafen, Germany) was used for dispersion of TiO₂.

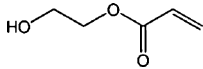
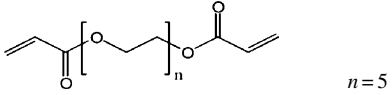
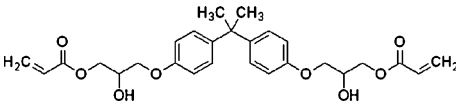
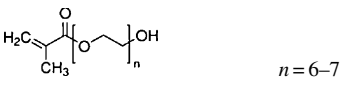
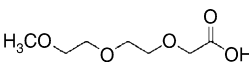
Genocure LTM, a liquid photoinitiator blend with a broad absorption peak around 380 nm from Rahn, Switzerland was used as the photoinitiator. LTM contains about 25% of TPO (2,4,6-trimethyl-benzoylphenyl-phosphineoxide).^{23–26}

2.2. Ink preparation and characterization

The monomers, surfactants and powders are mixed in 50 ml agate vessels containing 1 mm and 10 mm ZrO₂ milling balls. The pastes are homogenized in a planetary mill (PM 400, Retsch, Germany) at 250 rpm for 15 min. The ratio of powder to monomer was kept 1:1 wt/wt at this stage. The rest of the powder is added gradually to the paste along with appropriate amount of surfactant and the paste is homogenized again at 250 rpm for 15 min. After the addition of all the powder, the paste is milled for an additional 3 h at 350 rpm. In this ‘milling’ process the Al₂O₃ and HA agglomerates are broken down to the primary particle size but no actual reduction in particle size occurs.

The inks (particle type, resin and surfactant) studied in this work are listed in Table 2. The solid loading of the ceramic

Table 1
Monomers and surfactants used in this work for ink preparation.

Chemical	Manufacturer	Function	Density (25 °C) (g/cm ³)	Formula
4-Hydroxybutyl acrylate (4-HBA)	BASF, Germany	Monomer	1.04	
Polyethylene glycol (200) diacrylate (PEGDA)	Rahn, Switzerland	Monomer/oligomer	1.12	
Bisphenol A diacrylate (BPADA)	Sigma-Aldrich, Switzerland	Monomer	1.18	
Polyethylene glycol methacrylate (PEGMA) (360 g mol ⁻¹)	Sigma-Aldrich, Switzerland	Monomer/oligomer	1.105	
2-[2-(2-Methoxyethoxy) ethoxy] acetic acid (TODS)	Sigma-Aldrich, Switzerland	Surfactant	1.161	

particle in the monomer is given as both weight and volume fractions. TODS (wt% per weight of powder) was 1% for Al₂O₃ and 3% for HA. The approach explored to achieve printable inks is discussed in Section 3.1. The exact composition of the three inks which were printed by robotic deposition is indicated in bold (Table 2).

The particle size distribution (PSD) of the Al₂O₃ based dispersion was measured with a Beckman Coulter LS230 (USA) equipped with polarization intensity differential scattering (PIDS) for reliable analysis in the submicron range. The PSD found for electrostatically stable dispersions in aqueous media was used as a reference for a well dispersed system. The pastes were first lightly mixed with a large amount of DI water (no dispersion tool was used) and the PSD was measured in DI water.

Shear viscosity measurements for inks I–III were performed with a rotational viscosimeter (Rheolab MC 120, Physica Messtechnik GmbH) at 20 °C. Homogenization of the dispersion at 10 s⁻¹ for 3 min is done before each measurement. The measurement is repeated three times and consists of 20 measurement points from 10 to 1000 s⁻¹ with a logarithmic progression of shear rate. Values from the third measurement (which was essentially similar to the second measurement) are reported.

The viscosity of inks IV–VII was measured at 23 °C with a Paar Physica MCR 300 (Anton-Paar, Germany) with a parallel plate system (diameter = 50 mm, gap = 0.5 mm) in ascending and descending modes. The ascending measurement consisted of 5 equilibration points at 1 s⁻¹, 10 logarithmically spaced points between 1 and 500 s⁻¹ and 5 equilibration points at 500 s⁻¹ with

Table 2
Ink compositions studied in this work.

Ink	Approach	Resin composition	Solid loading (wt%/vol%)	TODS (wt% per weight of powder)
I (Al ₂ O ₃)	High solid loading dispersion	4-HBA/PEGDA (14:1)	82.5/55	1
II (Al ₂ O ₃)	High solid loading dispersion + high viscosity monomer	4-HBA/BPADA (1:1)	82.5/56	1
III (Al ₂ O ₃)	Oligomer	PEGDA	65–78.5/34–49 Printed: 75/45	1
IV (Al ₂ O ₃)	Oligomer	PEGMA/PEGDA (1:1 or 9:1) Printed: (1:1)	75/45	1
V (HA)	Oligomer	PEGDA	40/19	3
VI (HA)	Oligomer	PEGMA	43/21	–
VII (HA)	Oligomer	PEGMA/PEGDA (9:1) Printed: 59/32	59–62/32–35	3

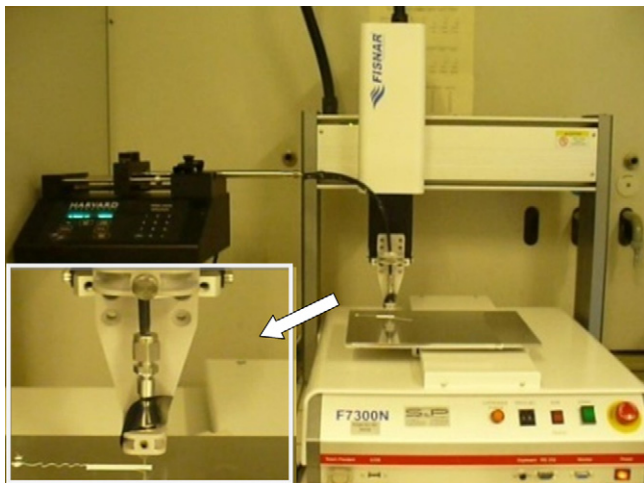


Fig. 1. The 3d robotic printing system used in this work.

6 s between measurement points. Most inks showed thixotropic behavior. The descending leg is reported.

The storage modulus of the inks at 23 °C was measured by oscillation rheometry (amplitude sweep) with a similar parallel plate system (Paar Physica MCR 300, Anton-Paar, Germany). This was done immediately after the viscosity measurement. During the tests a time independent shear deformation was measured at a controlled shear stress (40 points with a logarithmic progression from 1 to 500 Pa) at a frequency of 1 Hz.

In one experiment the storage modulus (G') was measured before and after the viscosity measurement.

The photoinitiator in an amount of 1% (for inks VI–VII) and 3% (inks I–III) per resin is added to the paste and mixed thoroughly. The UV curable inks are stored in glass/plastic vessels covered with aluminum foils until use.

2.3. 3d robotic deposition and curing

The 3d robotic deposition system is shown in Fig. 1. It consists of an extrusion system delivering the ink and a robot equipped with an y table. The extrusion system consists of an 8 ml stainless steel syringe (Hamilton, USA) delivering the paste through a 20 cm (ink IV and VII) or 28 cm (ink III) long, flexible PTFE tube to a luer-lock connection fixed to the dispensing robot head which is capable of moving in the x and z axes. The syringe is driven by a precision syringe pump (PHD 2000, Harvard Scientific, USA). The pump allows a pressure drop of up to 30 Bar in such an extrusion system.

The robot (Fisnar I&J 7300) is a 3 axis dispensing robot having a 300 mm \times 200 mm plate where the 3d fiber networks are deposited. A 160 μm or 210 μm (12.5 mm straight tip) or 200 μm (conic tip) dispensing die is connected to the fixed luer-lock connection. The z position of the robot head was programmed so that the dispensing tip was positioned 400–500 μm above the plate (or subsequently the last deposited layer). The inks were transferred to the 8 ml syringe through a 100 μm sieve in order to remove large particles and agglomerates which could block the needle. The printing of all pastes was conducted during continuous extrusion at room temperature. For ink III the

volumetric rate of 0.01 ml min⁻¹ was used (corresponding to a 160 μm filament linear deposition velocity of 8.3 mm s⁻¹). Ink VII was extruded through a 200 μm die at 0.2 ml min⁻¹ and ink IV through a 210 μm die at a volumetric rate of 0.04 ml min⁻¹. Inks IV and VII were printed at a robot translation velocity of 12 and 60 mm s⁻¹, respectively. Due to electrostatic effects the deposition was done on an aluminum foil. The cured fiber network could be easily removed from the foil for subsequent processing.

The UV curing was done with a hand held 100 W UV lamp (UVhand100, Dr. Hönle AG, Germany) producing 120 mW cm⁻² in the UVA spectrum (100 W Fe bulb).^{23–26} The deposition was interrupted after a deposition of 2 layers and the UV lamp was positioned above the freshly deposited structure for 2 min (dose of 14.4 J cm⁻²).

2.4. Transformation to macroscopic ceramics and functionalization

The cured 3d fiber networks or films were debinded in air by heating at 1 °C min⁻¹ to 600 °C and a soak of 1 h at 600 °C. Partial densification was carried out between 1200 and 1300 °C for 1 h and 1300 °C for 1 h, for HA and Al₂O₃, respectively, followed by 15 h cooling to room temperature.

The procedure of functionalization involved dip coating of sintered 2-layer periodic Al₂O₃ lattices in an aqueous 15 wt% TiO₂ nanoparticle dispersion stabilized with 10% (per weight of particle) Melpers4343 comb-polyelectrolyte surfactants. The detailed procedure for the preparation of the dispersions is described elsewhere.²⁵ The samples were pulled out of the dispersion at a constant rate of 1 mm s⁻¹ using the programmed robot (Fisnar I&J 7300, Fisnar, USA). The coated materials were placed and dried overnight in a 60% RH desiccator. The surfactant was removed by heating at 1 °C min⁻¹ and soaking at 500 °C in air for 1 h. The weight of TiO₂ deposited on the Al₂O₃ lattices was determined by measuring the weight gained after the soak at 500 °C.

2.5. Characterization of 3d structures

Ceramic and ceramic/polymer composite fibers were characterized by optical microscopy (Zeiss discover V8) and SEM (VEGA Plus 5136 MM, Tescan instruments, Czech republic). Selected multilayered samples were embedded in epoxy resin and polished. The procedure consisted of plane grinding with 20 μm diamond disc under water, fine grinding on SiC grinding paper P1000 and P2500. This followed by polishing on a MD Nap cloth with 3 μm diamond suspension DP, 1 μm DP and finally on MD Chem cloth with colloidal silica suspension OP-U.

The photocatalytic activity of functionalized 2d structures and loose TiO₂ powders for the decomposition of formaldehyde was performed by injection of 0.0002 ml formaldehyde via a septum to a glass tube containing 2.5–6 mg of supported catalyst or 3–7 mg of loose powder catalyst. The samples were irradiated for 1 h in an UV cabinet equipped with UVA lamps (Philips TL

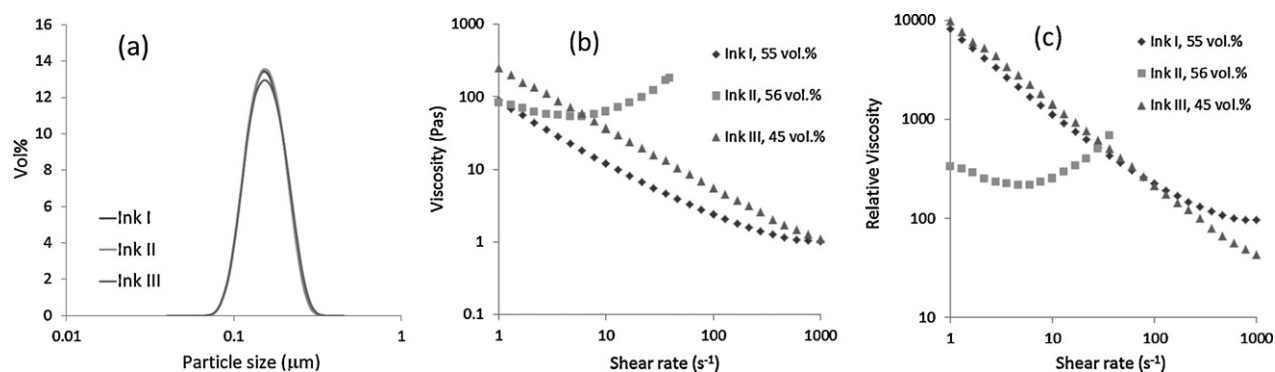


Fig. 2. Characteristics of UV curable colloidal Al_2O_3 inks I–III. (a) psd, (b) apparent viscosity, and (c) relative viscosity.

4 W/05 FL tube) with a maximum intensity at 365 nm.²⁸ To test for possible catalytic effects blank samples were stored in the dark in a drying oven at 28 °C as a reference. However, no such effect was detected. The amount of unreacted formaldehyde was determined in all samples by a procedure outlined elsewhere using photometric measurement of compounds prepared by the Hantzsch procedure.²⁸

3. Results and discussion

3.1. Development of radiation curable inks

An ideal ink should meet a long list of requirements. First and foremost, it needs to be UV curable, extrudable at room temperature under moderate pressure while maintaining the shape of the printing nozzle; be homogeneous with a high concentration of colloidal particles enabling the transformation of the cured nanocomposites to macroscopic ceramics. Less critical, yet important considerations are the ability to handle the ink (sieving and filling, electrostatic effects) and the cured fiber composites (de-molding, folding/cutting, firing).

Several approaches to obtain printable inks with adequate viscoelastic properties from solvent free, monomer based systems were attempted in the present work: (a) maximization of solid loading, (b) use of high viscosity monomers, and (c) use of low viscosity oligomers. Additives such as soluble polymers and alternative surfactants were also explored for HA but these inconclusive results will not be included in the discussion.

3.1.1. Al_2O_3 inks (I–III)

Table 2 lists the ink compositions studied in this work. For sake of clarity, the Al_2O_3 colloidal inks I–III will be discussed first. The surfactant used in all pastes was TODS (Table 1). TODS provides electrosteric stability²⁷ and is compatible to all the monomers/oligomers used in this study via its ethylene oxide (EO) backbone. Ink I is a monomer system which was studied in the past in detail for spinning and UV curing ‘on the fly’.^{23–26} At a solid loading of 42 vol% the viscosity is in the order of 0.2 Pas (500 s^{-1} , 23 °C) and it is necessary to spin the dispersions into a liquid in order to obtain continuous filaments. In the present work, the solid loading was increased from 42 vol% up to 55 vol% in order to increase particle–particle interactions. Ink

II contains 56 vol% powder (Table 2) and the resin consists also of high viscosity BPADA monomer (Table 1). Ink III contains 45 vol% powder with only PEGDA. This monomer/oligomer consists of two acrylate groups spaced by 5 EO groups (therefore the term oligomer is more appropriate here). Fig. 2 presents the characteristics of the inks. The PSD of the inks diluted in DI water shows a mono-modal distribution around 160 nm corresponding closely to the Al_2O_3 (TMDAR) particle size (Fig. 2a). Fig. 2b shows the apparent viscosity of the three inks. The three inks show quite different rheological behavior. Inks I and III show strong shear thinning behavior (power law index of ~ 0.2 up to 100 s^{-1}) whereas ink II shows shear thickening behavior above about 10 s^{-1} , a property undesirable for 3d printing applications. Ink I starts to show an onset of shear thickening as well, but only at much higher shear rates ($\sim 1000 \text{ s}^{-1}$). At 1 s^{-1} inks I and II exhibit somewhat lower viscosities compared to ink III. However, when the relative viscosity is considered by dividing the viscosity of the ink by that of the monomer (Fig. 2c) inks I and III show very similar values up to $\sim 100 \text{ s}^{-1}$.

It is worthwhile to note that ink I contains 55 vol% particles whereas ink III only 45 vol%. This indicates that particle–particle interactions dominate the rheological behavior of ink III at much lower solid loadings compared to ink I. Although it has the highest solid loading of 56 vol% the relative viscosity of ink II at 1 s^{-1} is a factor of 30 lower than that of inks I and III, indicating a much larger contribution of the monomer to the apparent viscosity.

Fig. 3a shows the storage modulus (G') of inks I–III. Despite their higher solid loading inks I and II have storage moduli which are a factor of 35 and 90 lower than that of ink III, respectively. Ink II also exhibits a relatively low yield point. Conversely, the addition of high viscosity monomers such as the H-bonding BPADA results in a shear thickening behavior rather than an increase in storage modulus.

G' (or the yield stress) can be expressed by y in Eq. (1)⁴:

$$y = k \left(\frac{\phi}{\phi_{\text{gel}}} - 1 \right)^n \quad (1)$$

where ϕ and ϕ_{gel} are the volume fraction and minimal volume fraction where gel is formed, respectively, n is an exponent (typically 2.5)⁴ and k is a constant which is system specific. If the volume fraction stays constant, the constant k can be viewed

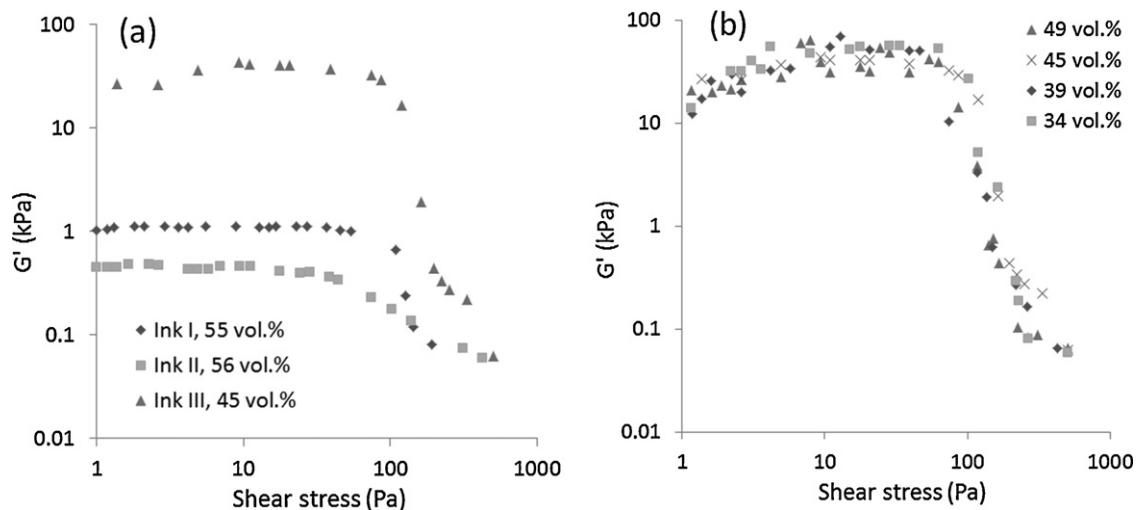


Fig. 3. Storage modulus (G') of UV curable colloidal Al_2O_3 inks. (a) Inks I–III, (b) ink III at solid loadings between 34 and 49 vol.%.

as the strength of particle–particle interaction which may be induced for example by a variation of pH or solvent quality.⁴

The results in Figs. 2 and 3a indicate that despite the apparent homogeneity of the ink (PSD in Fig. 2a) its rheology is dominated by particle–particle interactions. Such strong interactions could not be induced in inks I and II by increasing the solid loading to 55–56 vol%. In the 4-HBA medium the TODS acts as an efficient surfactant. However, since the backbone of both TODS and PEGDA is built of EO units (Table 1) the surfactant and medium are compatible, but indistinguishable. Therefore effective steric barrier is not established. For the Al_2O_3 particles studied here this situation leads to an ink which is both printable and homogeneous.

Preliminary printing experiments with inks I and II show poor shape retention of the filaments. Further increase in solid loading in ink I above 55 vol% may lead to printable inks but the transition from shear thinning to shear thickening behavior in these ‘over-stabilized’ systems occurs in a very narrow concentration window, and therefore extremely difficult to control in practice. Therefore, only ink III was considered further

for robotic deposition. Fig. 3b shows the storage modulus of ink III with solid loading ranging from 34 to 49 vol%. Interestingly, in this relatively large solid loading range, the storage modulus is mostly independent of the solid fraction, indicating particle–particle interaction dominates the system already at low solid loading. Some small differences at the low shear stress range can be observed. The G' values observed here for ink III are in the order of 4×10^4 Pa. These are within the lower range of the values reported by Smay et al. and Lewis.^{4,5} It is important to note that the measurements of G' were done after the inks were pre-sheared at 500 s^{-1} since this corresponds better to the situation where the extruded filament exits the die. In one experiment where G' was measured before and after the pre-shearing step, the value of G' before the pre-shear step was an order of magnitude higher, indicating significant relaxation effects.

3.1.2. HA inks (V–VII) and Al_2O_3 ink IV

The PEGDA/TODS combination used for Al_2O_3 in ink III showed similar benefits for HA (ink V) in comparison with 4-HBA based compositions. The storage modulus of $\sim 10^5$ Pa was

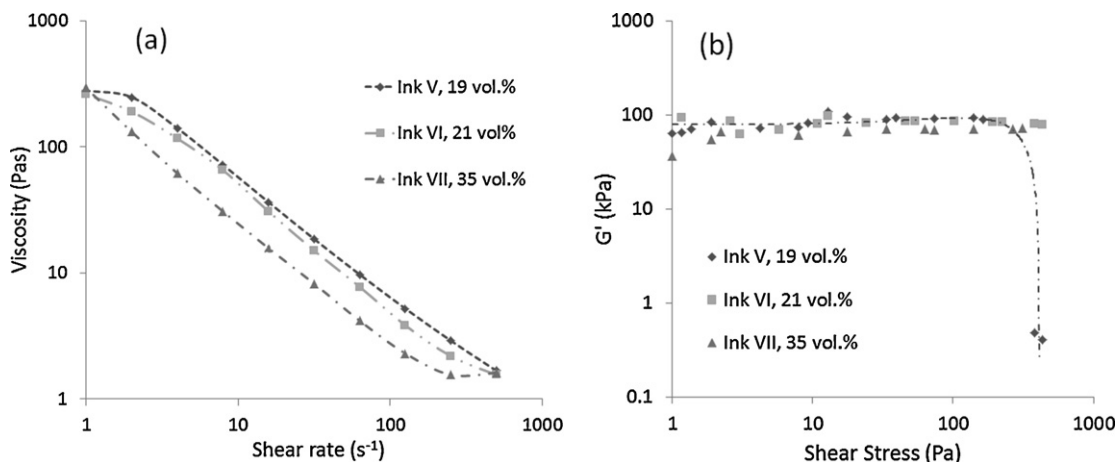


Fig. 4. Viscosity and storage modulus of UV curable colloidal HA inks V–VII. (a) Apparent viscosity, (b) storage modulus (G'). The fit to the storage modulus of ink V is given only as a guide to the eye.

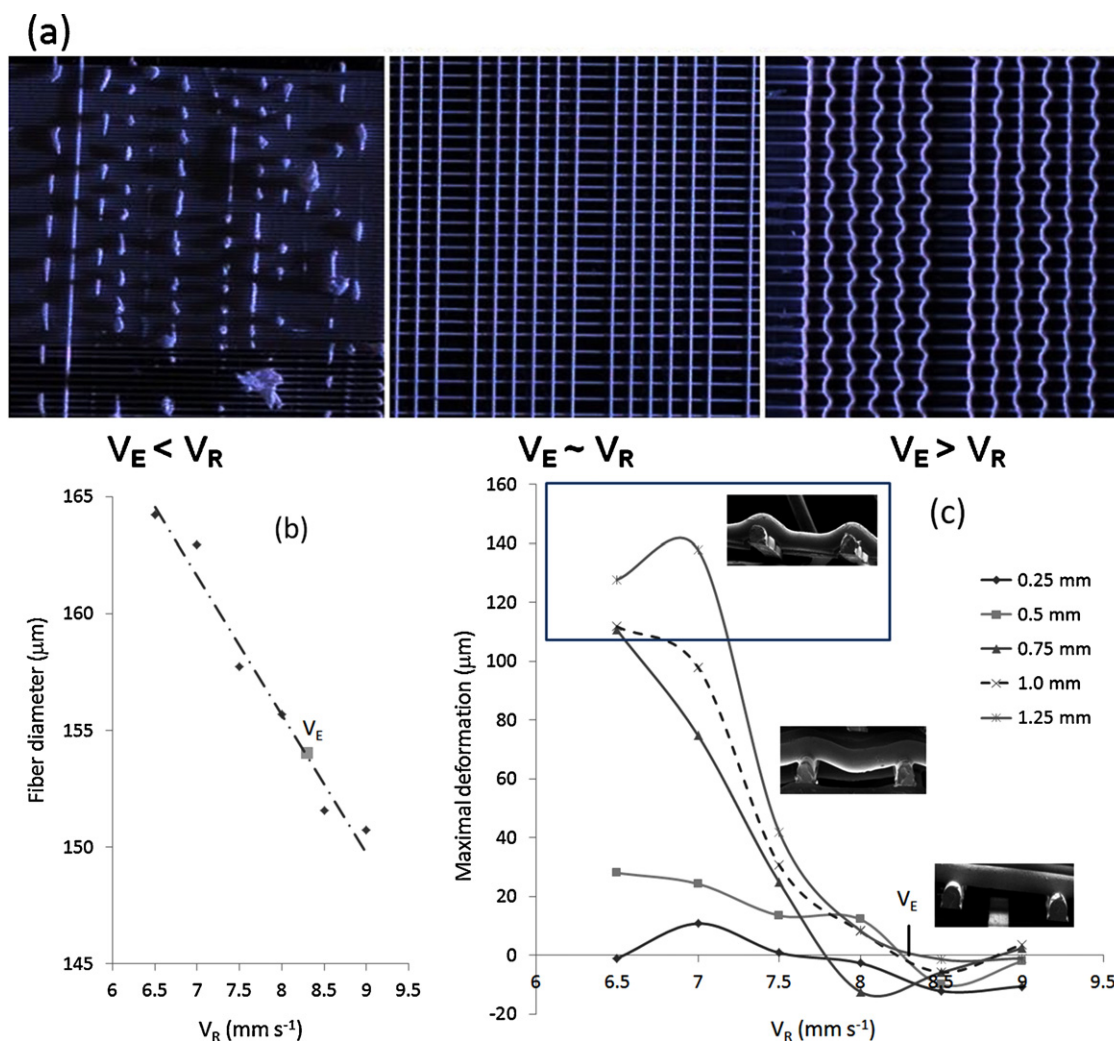


Fig. 5. Characterization of the printing process of ink III through a $160 \mu\text{m}$ die at a fixed linear extrusion velocity (V_E) of 8.3 mm s^{-1} . (a) Effect of robot translation velocity (V_R) on the deposition of second layer fibers (top view); (b) effect of robot translation velocity on the diameter of fibers deposited in second layer; and (c) effect of robot translation velocity and first layer fiber to fiber spacing on the deformation of fibers deposited in second layer.

found with viscosity suitable for printing (Fig. 4). Nevertheless, due to the relatively high SA of the HA powder ($67 \text{ m}^2 \text{ g}^{-1}$ compared to $12.5 \text{ m}^2 \text{ g}^{-1}$ for Al_2O_3) the maximal HA solid loading which could be extruded in the system was limited to only 19–21 vol%. As in the case of Al_2O_3 additions of 4-HBA have resulted in a significant increase in the dispersed HA fraction (up to 35% at a 4-HBA/PEGDA ratio of 2:1), but this was similarly accompanied with a reduced G' ($G' \sim 5 \times 10^3 \text{ Pa}$ at 62.5 wt%) and shape retention. New monomer/oligomer combinations were necessary to produce printable HA inks with higher solid loading. PEGMA, a monofunctional oligomer (Table 1) which has 6–7 EO units separating its methacrylate and OH functionalities provides an interesting choice since it is comparable in length to the PEGDA and in polarity of the OH group to 4-HBA. Fig. 4 shows that such an oligomer when used without TODS (ink VI) produces similar results (storage modulus and solid loading) to a PEGDA/TODS system (ink V). This suggests that monomer length effects dominate the interactions for these particle compatible systems. However, the PEGMA/PEGDA (9:1)/TODS system enables increasing the solid loading close to

the level seen with 4-HBA, while maintaining viscosity suitable for printing (Fig. 4a) without a large penalty in G' (Fig. 4b). Here, the effect of oligomer length and chemistry is clearly distinguished. The significantly higher solid loading is enabled, as in the case of 4-HBA, by the increased efficiency of TODS as steric dispersant due to synergy of the EO groups with the OH terminated monomers. As discussed previously, in PEGDA such effects are small due to the similarity in the EO structure. At the same time, the high G' (about $7 \times 10^4 \text{ Pa}$ for ink VII) is primarily attributed to the effect of the increased length of the PEGMA compared to 4-HBA. Ink VII is therefore selected for printing. However, unlike the case with ink III it provides a relatively narrow concentration window (3–4 wt%) where extrudable inks having good shape retention can be obtained. In addition, the HA inks show even stronger shear thinning effects than Al_2O_3 with a power law index between 0 and 0.08 (Fig. 4a). We also find that the resin composition (PEGMA/PEGDA) could be adapted for the Al_2O_3 system (1:1, ink IV). Due perhaps to the lower SA this has a much smaller effect on the maximal solid loading and rheology of the ink. The 1:1 paste shows continuous extrusion

with low electrostatic effects and pressure drop compared to ink III.

A better insight into the rheology of both Al_2O_3 and HA oligomer systems is currently sought after using rheological models.^{29,30}

3.2. Robotic deposition of 3d fiber networks

3.2.1. Characterization of the 3d deposition process (ink III)

To demonstrate the robotic deposition of the new inks, lattices with a fiber to fiber spacing between 0.25 and 1.25 mm were selected. The optimal conditions for deposition of second or higher order layers were determined in one experiment where the first deposited layer consisted of regions having fiber spacing of 0.25, 0.5, 0.75, 1.0 and 1.25 mm. The second layer was deposited on top of the first at a constant volumetric deposition rate of $0.01 \text{ cm}^3 \text{ min}^{-1}$. For the $160 \mu\text{m}$ tip used in all experiments with ink III this corresponds to a linear filament extrusion velocity (V_E) of 8.3 mm s^{-1} . The deposition of the second layer was studied in a range of robot translation velocities (V_R) between 6.0 and 10 mm s^{-1} . The velocity was varied after deposition of several fibers across the first layer in 0.5 mm s^{-1} increments. Fig. 5 shows the results of this characterization experiment. Three distinct regions are identified in Fig. 5a where the shape of the fibers deposited in the second layer is observed (top view). At high translation velocities ($V_E < V_R \sim 9.5 \text{ mm s}^{-1}$) the deposition of fibers becomes discontinuous due to tearing of the filaments, whereas at low translation velocities ($V_E > V_R \sim 6.0 \text{ mm s}^{-1}$) the fibers are no longer deposited in a linear path due to large excess of extruded material. At intermediate velocities ($V_E \sim V_R$) the continuous fibers are deposited in a linear path. Nevertheless, the condition of linearity does not guarantee optimal deposition. Samples from the intermediate region of Fig. 5a which correspond to different translation velocities were further analyzed by SEM. The average diameter of the fibers and the ‘maximal deformation’ are presented in Fig. 5b and c, respectively. The maximal deformation is a measure of the degree at which the fiber in the second layer is deformed in the z axis. It is defined as the vertical distance from the top of the first layer to the bottom of the second layer.

Fig. 5b shows that at a given linear extrusion velocity, the average diameter of the fibers is dependent on the robot translation velocity. These values are also dependent, but to a lesser degree, on the spacing of the first layer. Thus, the values have been averaged for clarity. At the estimated nominal extrusion velocity $V_R \sim V_E = 8.3 \text{ mm s}^{-1}$ the average diameter of the fibers is $154 \mu\text{m}$, perhaps indicating a small shrinkage of the nominal filament (die ID of $160 \mu\text{m}$) during curing. Within the intermediate region (Fig. 5a) the fiber may be either slightly stretched at higher translation velocities ($V_R > V_E$) or compressed when ($V_R < V_E$).

The fiber deformation behavior shown in Fig. 5c can be divided into three regions. The SEM images provided in Fig. 5c illustrate the typical fiber structures in each region. In the first ($V_R > 8.0 \text{ mm s}^{-1}$) the measured value of deformation is around $0 \pm 10 \mu\text{m}$ (which is within the error of measurement)

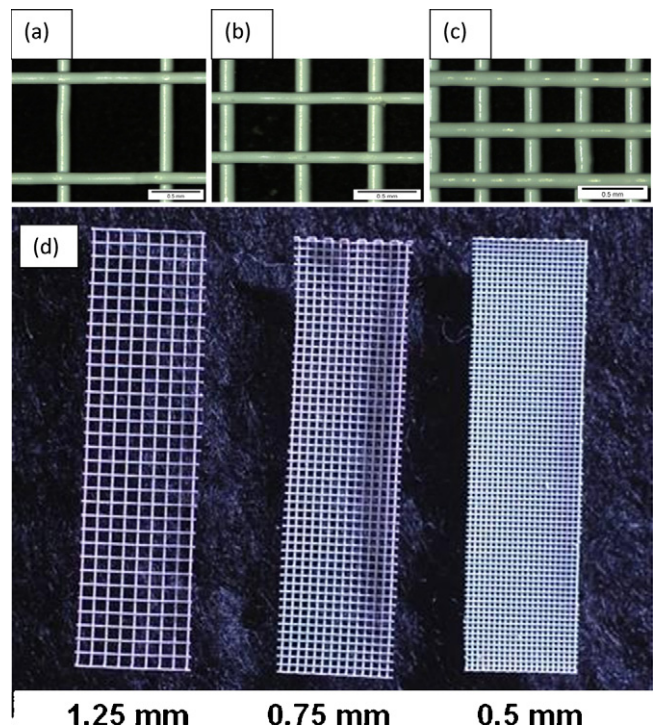


Fig. 6. (a–c) Cured 2-layer periodic Al_2O_3 nanocomposite lattices produced by printing and UV curing (ink III). Fiber to fiber spacing is 1.25 mm (a), 0.75 mm (b), and 0.5 mm (c). Scale bar is 0.5 mm. (d) Sintered Al_2O_3 2-layer periodic lattices which are $9 \text{ mm} \times 33 \text{ mm}$ in size. The samples in (d) were cut from printed periodic structures of area $40 \text{ mm} \times 80 \text{ mm}$ with spacing similar to those shown in (a)–(c).

irrespective of fiber spacing, indicating the deposition is optimal without (or with negligible) deformation of the filaments. In the second region ($7.0 < V_R < 8.0 \text{ mm s}^{-1}$) the deformation is highly dependent on the fiber to fiber spacing in the first layer. The fibers deposited at a spacing of 0.25 and 0.5 mm show little deformation when the translation velocity is decreased in this range, whereas fibers deposited on spacing $\geq 0.75 \text{ mm}$ show very sharp increase in deformation with decrease in translation velocity below 8.0 mm s^{-1} . In the third region (denoted by the frame in Fig. 5c), which is only observed for spacing $\geq 0.75 \text{ mm}$ at low translation velocities ($\leq 7.0 \text{ mm s}^{-1}$), the deformation is at its highest value and the fiber is partially deposited on the substrate at the level of the first layer.

3.2.2. Deposition of 2d and 3d architectures

Fig. 6a–c shows cured Al_2O_3 nanocomposite 2-layer periodic lattices with fiber to fiber spacing of 0.5, 0.75 and 1.25 mm, respectively, deposited with ink III at $V_R = 8.3 \text{ mm s}^{-1}$. Small sections which were cut out of large ($40 \text{ mm} \times 80 \text{ mm}$) lattices and sintered at 1300°C are shown in Fig. 6d. These high aspect ratio samples remain intact and show no major deformation or change in shape after the debinding and sintering processes.

Large, multilayered samples with periodic structure are produced from ink III by repeating the 2-layer deposition and curing steps multiple times. Fig. 7 (top) shows a section of sintered Al_2O_3 structure originally printed with 16 layers at a fiber spacing of 0.5 mm. The sintered fibers in the

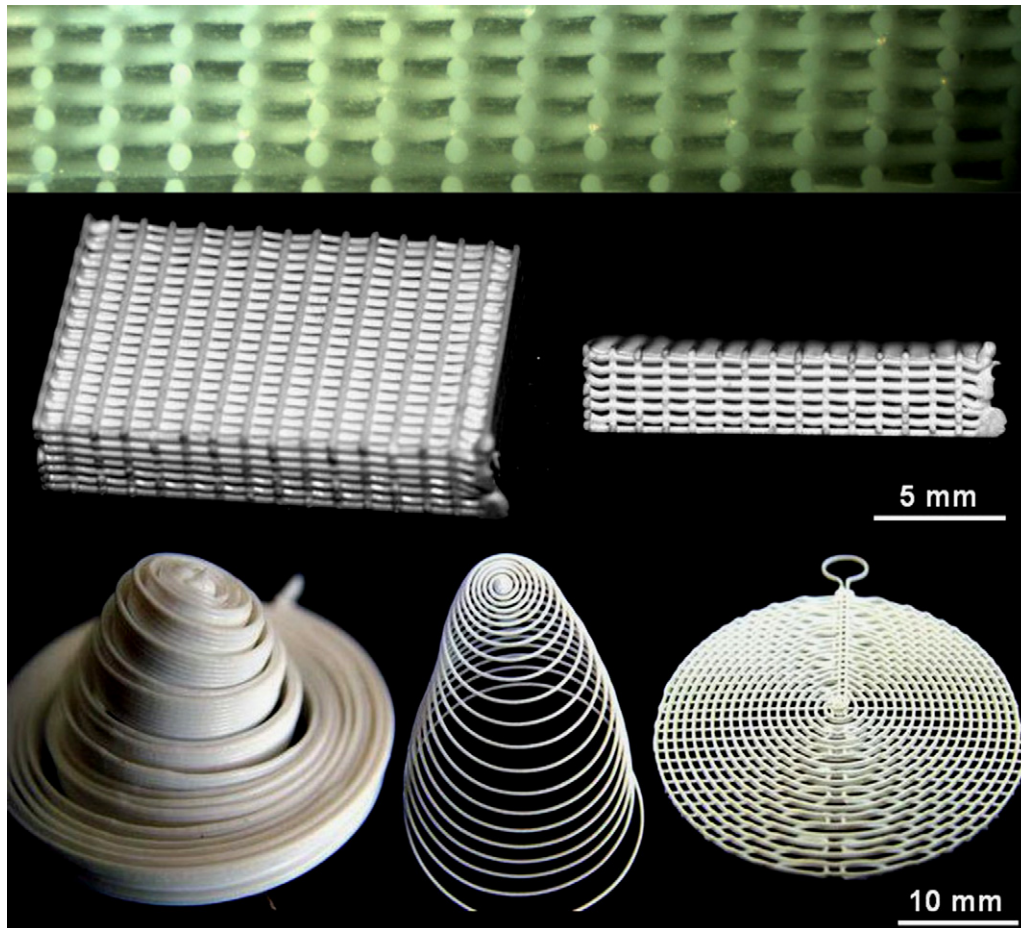


Fig. 7. Periodic multilayers and other printed architectures. *Top*: An embedded section of sintered Al_2O_3 periodic multilayer printed with 16 layers (ink III); fiber diameter is $\sim 125 \mu\text{m}$. *Bottom*: Cured periodic multilayers, simple and multilayered spiral architectures (ink IV). Average fiber diameter is $250 \mu\text{m}$. The spirals are stretched in the image.

intact multilayer structure are about $125 \mu\text{m}$ in diameter after sintering at 1300°C . Fig. 7 (bottom) demonstrates the possibility to produce periodic multilayers, single and multilayer spiral nanocomposite architectures, as well as a simple combination of the two. The structures in Fig. 7 (bottom) were deposited with ink IV (composition in bold Table 2) using a $210 \mu\text{m}$ die. The average fiber diameter here is $250 \mu\text{m}$ indicating velocity mismatch (Fig. 5b) and possibly die swell effects.

3.3. Post-printing processes

3.3.1. Shaping (folding, cutting and bonding)

Further shaping of printed structures by post-printing processes is desired to create new structures which are difficult or time consuming to print directly. Such manipulations may require for example cutting, reassembling and bonding. Shaping of printed structures by special post-printing processes has been proposed recently by Ahn et al.¹⁹ who printed TiH_2 inks containing a mixture of solvents. A fast evaporating solvent provides fast shape stabilization and the slow evaporating solvent allows for flexibility of the structure during folding operations. The folded structure thus produced is ‘fixed’ as it hardens during

the evaporation of the slow evaporating solvent. In contrast to such inks, the cured HA/polymer and Al_2O_3 /polymer nanocomposite lattices are flexible without the use of solvents and can be easily shaped to various 3d architectures by post-printing processes such as bending, folding/rolling, cutting, re-assembling and bonding. The structures can be fixed with a specific internal/external mold during debinding and sintering. Due to the lack of hardening mechanism, fixing of more complex structures cannot be done as described by Ahn et al.¹⁹ Nevertheless, UV curable fiber layers can be deposited before or after folding in the interface where bonding is required and the structure is fixed by UV irradiation. Fig. 8 shows a simple scheme used here for creating 3d structures by post-printing processes. First, spacer layers are deposited on a cured 2-layer periodic lattice structure (Fig. 8, left). Several spacer layers can be deposited and cured on top of each other. In a second step, the structure is folded/rolled (Fig. 8, right) and inserted into a cylindrical crucible which maintain its shape during firing. Alternatively, the top layer may be left uncured and cured while or after the folding operation, in order to prepare a self-supporting 3d composite structure.

Fig. 9a and b shows several sintered HA structures which were produced by bending or folding/rolling of 2-layer

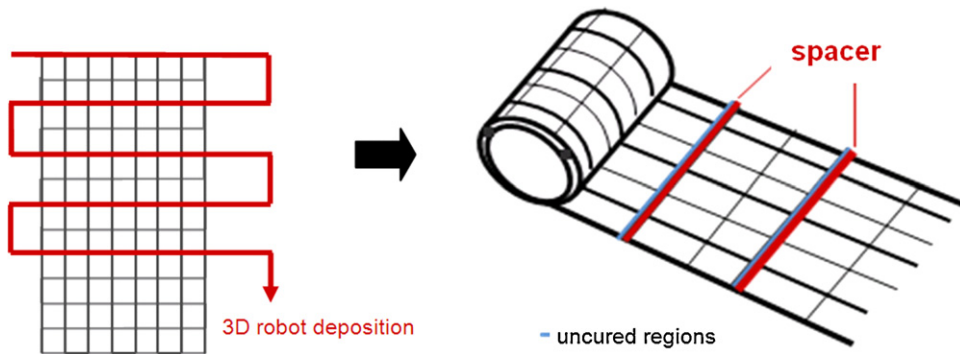


Fig. 8. Scheme for producing simple 3d architectures from 2-layered periodic lattices. Deposition of spacer layers (left), folding/rolling and optionally bonding to produce 3d structure (right).

periodic lattices according to Fig. 8. The simple bending operation was done around circular alumina molds. Fig. 9b highlights the cross section of the folded structures seen in Fig. 9a with (top) or without spacers (bottom). The flexible

nanocomposite structures which are 10 cm in length could be easily rolled into densely packed structures and fixed into shapes which transform to sintered structures with a radius of 3–4 mm (Fig. 9b).

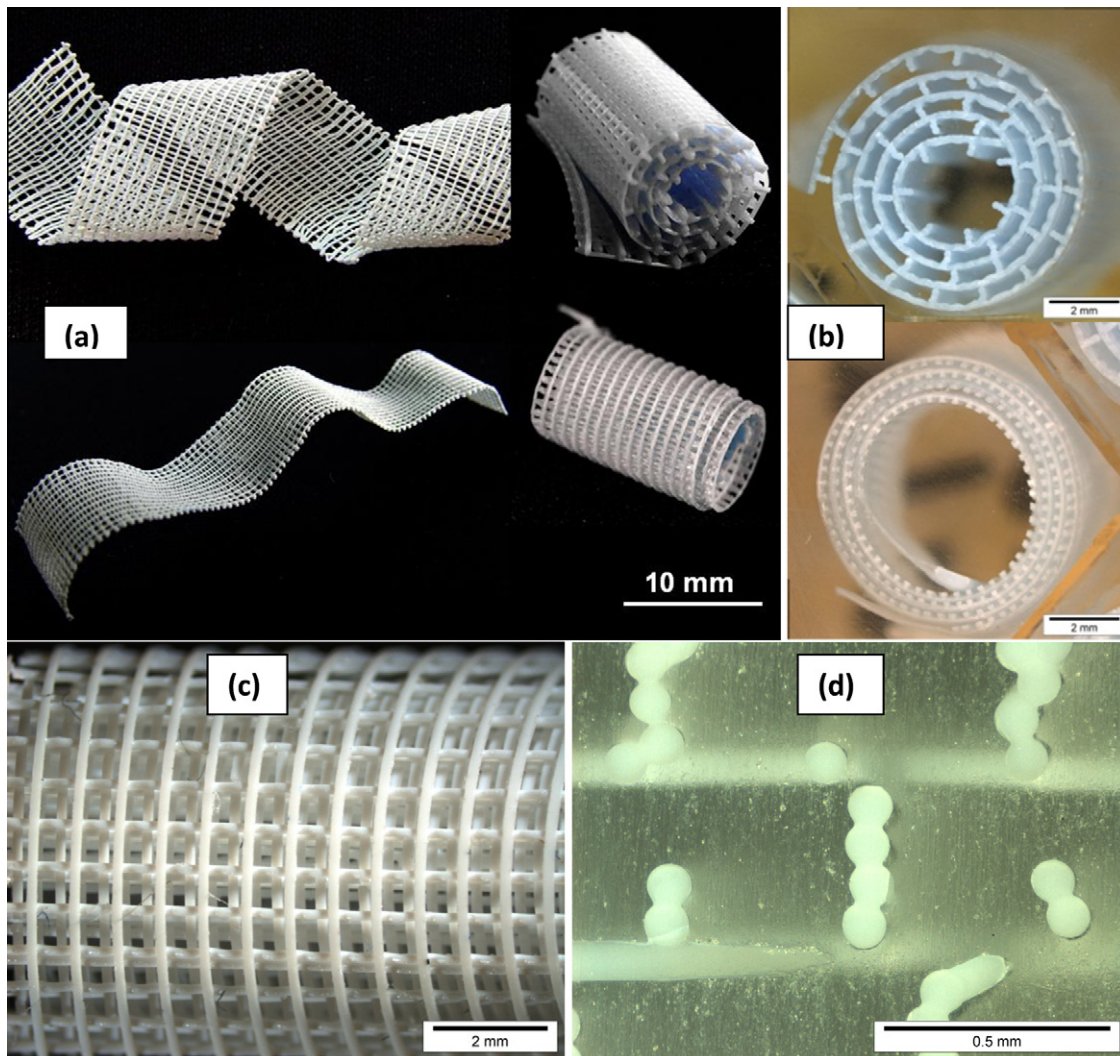


Fig. 9. Various 3d structures prepared by post-printing manipulation of 10 cm long 2-layered periodic lattices with or without printed spacers. (a and b) Sintered bent and folded/rolled HA structures (paste VII, 1250 °C), (b) embedded cross section of rolled structures in (a); right) produced by the scheme of Fig. 8; (top) with spacers, (bottom) without spacers. (c) Cured Al_2O_3 folded/rolled and bonded structure produced with a spacer by the scheme of Fig. 8 (ink III), (d) embedded sintered Al_2O_3 structure with three spacers and one bonding layer prepared by stacking and bonding of sections cut off a 2-layered periodic lattice structure (ink III).

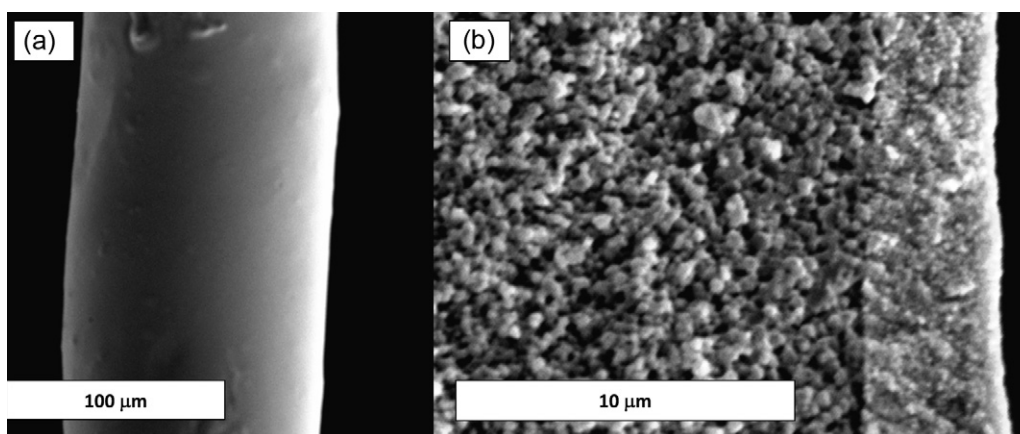


Fig. 10. 2-Layered periodic Al_2O_3 lattice functionalized with TiO_2 nanoparticles. (a) Functionalized fiber surface, (b) functionalized fiber cross-section.

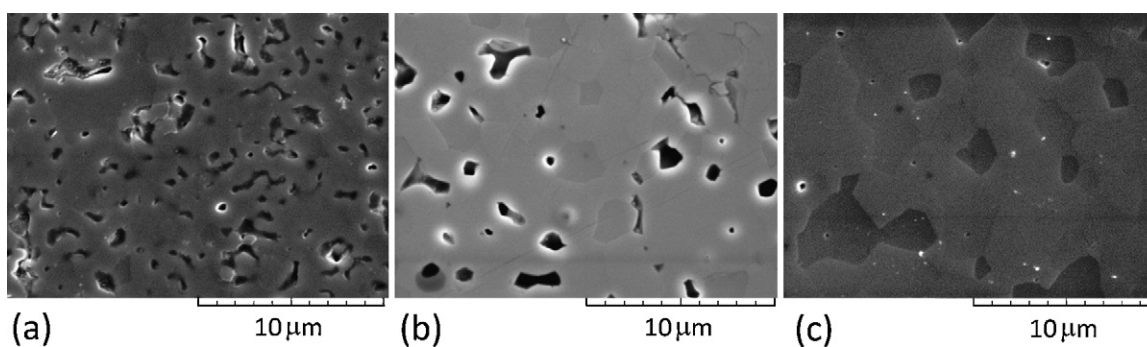


Fig. 11. Printed HA structures from ink VII sintered at various temperatures for 1 h: (a) 1200 °C, (b) 1250 °C, and (c) 1300 °C.

The color of the sintered HA structures produced in this work has a bluish tint which increases with sintering temperature. This stems most likely from small amounts of impurities (e.g. Mn) which lead to the development of color centers.³¹ It is also important to note here that inks IV–VII show small surface cracks after curing which is likely attributed to oxygen inhibition reaction resulting from the use of mono (meth)acrylates.³² Fibers prepared from ink VII and cured under argon flow show smooth surfaces before and after sintering but those cured in air reveal large growth of surface cracks after sintering.

An Al_2O_3 nanocomposite folded structure assembled and bonded as described in Fig. 8 is shown in Fig. 9c. In addition, a sintered structure which was printed, cut and UV bonded with an uncured layer on top of three cured spacer layers is seen in Fig. 9d. The uneven pressure induced during the assembly and bonding operation has resulted in deformation of several spacer layers. Such exemplary operation can be automated with improved control and precision.

3.3.2. Microstructure, coating and functionalization

The ability to produce structural Al_2O_3 structures with precisely defined architectures and high surface area to volume ratios may be interesting for applications as catalyst supports in prototype reactors.¹² As a simple demonstration for such potential applications the 2-layer periodic lattices which were partially densified at 1300 °C (shown in Fig. 6) were functionalized with a layer of TiO_2 nanoparticles. Similar approach was used by Plesch et al. to functionalize Al_2O_3 foams with TiO_2 .³³

Fig. 10a and b shows SEM images of a TiO_2 functionalized Al_2O_3 fiber surface and a part of its cross section, respectively. A homogeneous and relatively dense TiO_2 layer which is 3–4 μm thick can be seen (Fig. 10b). Due to surface tension effects in the dip coating process, the thickness of the TiO_2 coating varies on the 2-layer periodic lattices. Thicker coating which shows cracks (leading sometimes to complete delamination) is found in regions where fibers from the first and second layers intersect, whereas smooth and continuous coatings are seen elsewhere (Fig. 10a). The functionalized 2-layer periodic lattices showed photocatalytic activity for the decomposition of formaldehyde similar to that of loose TiO_2 powder of similar TiO_2 mass.

Fig. 11 shows SEM images of polished surfaces of printed HA structures sintered at 1200 °C, 1250 °C and 1300 °C for 1 h. A gradual reduction in pore volume and corresponding increase in grain size can be seen with increased sintering temperature. Although some processing defects are present, treatment of 1 h at 1300 °C (Fig. 11c) seems sufficient for full sintering of HA derived from inks with 34 vol% and testifies to the homogeneity of the inks. Such sintering behavior appears to be similar to that observed by other researches which used other HA powder sources and binder systems.^{16,17}

4. Conclusions

Homogeneous, high loaded, monomer based, solvent free, UV curable colloidal Al_2O_3 and hydroxyapatite inks which exhibit good flow behavior and shape retention have been

developed by a proper selection of monomers/oligomers and surfactants. The rheological behavior of both particles studied exhibit similar dependency on the monomer systems studied but the effects are greatly diminished for the low surface area Al_2O_3 . The inks are printed by a new 3d robotic deposition technique where the printing and curing steps are decoupled. A variety of architectures such as high aspect ratio 2-layer periodic lattices, multilayers, single and multilayer spirals are printed successfully at a linear rate between 8 and 60 mm s^{-1} and cured to high loaded ceramic/polymer nanocomposites. The 2d nanocomposites thus formed are flexible and could be further shaped or assembled into ordered 3d structures by folding, cutting, re-assembling and bonding. The 2d and 3d nanocomposites transform to macroscopic ceramics via thermal debinding and sintering without delamination or distortion of the structure. Such versatile shaping platform is very promising for hydroxyapatite scaffolds. The functionalization of Al_2O_3 2-layer periodic lattices by a 3–5 μm thick TiO_2 nanoparticle layer which shows comparable photocatalytic activity to loose powder of similar mass was demonstrated using decomposition of formaldehyde as a model reaction.

Acknowledgments

The authors would like to thank Dr. Michalow, Empa, for the help with the photocatalytic experiments, and Evelyn Schlenker, Empa for help with sample preparation and polishing. The administrative support of Prof. Gorbunoff, HTWD and Prof. Graule, Empa is greatly appreciated. Jiri Misak wishes to acknowledge partial financial support of Cost action MP0701.

References

- Gibson I, Rosen DW, Stucker B. *Additive manufacturing technologies: rapid prototyping to direct digital manufacturing*. New York: Springer; 2010.
- Brady GA, Halloran JW. Stereolithography of ceramic suspensions. *Rapid Prototyping J* 1997;3:61–5.
- Chartier T, Duterte C, Delhote N, Baillargeat D, Verdeyme S, Delage C, et al. Fabrication of millimeter wave components via ceramic stereo- and microstereolithography processes. *J Am Ceram Soc* 2008;91:2469–74.
- Smay JE, Cesarano J, Lewis JA. Colloidal inks for directed assembly of 3-d periodic structures. *Langmuir* 2002;18:5429–37.
- Lewis JA. Direct ink writing of 3d functional materials. *Adv Funct Mater* 2006;16:2193–204.
- Huang T, Mason MS, Hilmas GE, Leu MC. Freeze-form extrusion fabrication of ceramic parts. *J Virtual Physical Prototyping* 2006;1:93–100.
- Duoss EB, Twardowski M, Lewis JA. Sol–gel inks for direct-write assembly of functional oxides. *Adv Mater* 2007;19:3485–9.
- Luyten J, Mullens S, Thijs I. Designing with pores—synthesis and applications. *KONA Powder Part J* 2010;28:131–42.
- Yang H, Yang S, Chi X, Julian R, Evans G. Fine ceramic lattices prepared by extrusion freeforming. *J Biomed Mater Res B: Appl Biomater* 2006;79B:116–21.
- Ravelingien M, Hervent AS, Mullens S, Luyten J, Vervaeck C, Remon JP. Influence of surface topography and pore architecture of alkali-treated titanium on in vitro apatite deposition. *Appl Surf Sci* 2010;256:3693–7.
- Van Noyen J, Mullens S, Snijders F, Luyten J. Catalyst design with porous functional structures. In: Reniers G, Brebbia CA, editors. *Sustainable chemistry, WIT transactions on ecology and the environment*, 154. WIT Press; 2011. p. 93–102.
- Stuecker JN, Miller JE, Ferrizz RE, Mudd JE, Cesarano J. Advanced support structures for enhanced catalytic activity. *Ind Eng Chem Res* 2004;43:51–6.
- Rao RB, Krafcik KL, Morales AM, Lewis JA. Microfabricated deposition nozzles for direct-write assembly of three-dimensional periodic structures. *Adv Mater* 2006;17:289–93.
- Moronia L, Schotel R, Sohler J, de Wijn JR, van Blitterswijk CA. Polymer hollow fiber three-dimensional matrices with controllable cavity and shell thickness. *Biomaterials* 2006;27:5918–26.
- Hutmacher DW, Sittinger M, Risbud MV. Scaffold-based tissue engineering: rationale for computer-aided design and solid free-form fabrication systems. *Trends Biotechnol* 2004;22:354–62.
- Michna S, Wu W, Lewis JA. Concentrated hydroxyapatite inks for direct-write assembly of 3-D periodic scaffolds. *Biomaterials* 2005;26:5632–9.
- Suwanprateeb J, Sanngam R, Panyathanmaporn T. Influence of raw powder preparation routes on properties of hydroxyapatite fabricated by 3D printing technique. *Mater Sci Eng C* 2010;30:610–7.
- Barry RA, Shepherd RF, Hanson JN, Nuzzo RG, Wiltzius P, Lewis JA. Direct-write assembly of 3d hydrogel scaffolds for guided cell growth. *Adv Mater* 2009;21:1–4.
- Ahn BY, Shoji D, Hansen CJ, Hong E, Dunand DC, Lewis JA. Printed origami structures. *Adv Mater* 2010;22:2251–4.
- Smay JE, Cesarano III J, Tuttle BA, Lewis JA. Directed colloidal assembly of linear and annular lead zirconate titanate arrays. *J Am Ceram Soc* 2004;87:293–5.
- Lebel LL, Aissa B, El Khakani MA, Therriault D. Ultraviolet-assisted direct-write fabrication of carbon nanotube/polymer nanocomposite microcoils. *Adv Mater* 2010;22:592–6.
- de Hazan Y, Graule T, Thänert M. 3d nano-composite and ceramic architectures via robotic deposition of UV curable inks. *Eur Cells Mater* 2011;22:35.
- de Hazan Y, Graule T, Müller G. Process and device for manufacturing shaped composite, the shaped composite and the shaped inorganic article derived from it. PCT/CH2009/000322, WO/2010/040243.
- de Hazan Y, Wozniak M, Heinecke J, Müller G, Graule T. New microshaping concepts for ceramic/polymer nanocomposite and nanoceramic fibers. *J Am Ceram Soc* 2010;93:2456–9.
- de Hazan Y, Märkl V, Heinecke J, Aneziris C, Graule T. Functional ceramic and nanocomposite fibers, cellular articles and microspheres via radiation curable colloidal dispersions. *J Eur Ceram Soc* 2011;31:2601–11.
- de Hazan Y, Heinecke J, Weber A, Graule T. High solids loading ceramic colloidal dispersions in UV curable media via comb-polyelectrolyte surfactants. *J Colloid Interface Sci* 2009;337:66–74.
- Straue N, Rauscher M, Walther S, Faber H, Roosen A. Preparation and soft lithographic printing of nano-sized ITO-dispersions for the manufacture of electrodes for TFTs. *J Mater Sci* 2009;14:6011–9.
- Ritter A, Reifler FA, Michel E. Quick screening method for the photocatalytic activity of textile fibers and fabrics. *Text Res J* 2010;80:604–10.
- Flatt RJ, Bowen P. YODEL: a Yield stress MODEL for suspensions. *J Am Ceram Soc* 2006;89:1244–56.
- Houst YF, Bowen P, Perche F, Kauppi A, Borget P, Galmiche L, et al. Design and function of novel superplasticizers for more durable high performance concrete (Superplast project). *Cem Concr Res* 2008;38:1197–209.
- Yubao L, Klein CPAT, Xingdong Z, de Groot K. Relationship between the colour change of hydroxyapatite and the trace element manganese. *Biomaterials* 1993;14:969–72.
- O'Brien AK, Bowman CN. Impact of oxygen on photopolymerization kinetics and polymer structure. *Macromolecules* 2006;39:2501–6.
- Plesch G, Gorbár M, Vogt UF, Jesenák K, Vargová M. Reticulated macroporous ceramic foam supported TiO_2 for photocatalytic applications. *Mater Lett* 2009;63:461–3.